J Solid State Electrochem (2007) 11:687–701
DOI 10.1007/s10008-006-0215-y

ORIGINAL PAPER

Copper deposition and dissolution in seemingly parallel electric and magnetic fields: Lorentz force distributions and flow configurations

C. Cierpka · T. Weier · G. Gerbeth · M. Uhlemann · K. Eckert

Received: 7 July 2006 / Accepted: 15 August 2006 / Published online: 11 October 2006

Abstract In two different cylindrical electrochemical cells, copper deposition and dissolution in the presence of a magnetic field mostly parallel to the electric field was investigated. Particle image velocimetry measurements show that even under such a field configuration where Lorentz forces are often a priori neglected may in fact dominate the flow. Further, depending on the electrode radius, a reversal of the secondary flow was found. This feature can be explained by the different Lorentz force configurations calculated from the magnetic field and the primary current distributions. The components of the magnetic field were determined by means of a traversed Hall probe and were calculated by a commercial finite element package. Experimentally and numerically determined field distributions match very well. A good agreement between the measured and calculated velocity distributions was also found, suggesting that in the present case the effect of the Lorentz force alone is sufficient to explain the magnetic field influence on the flow.

Contribution to the special issue "Magnetic field effects in Electrochemistry"

C. Cierpka · T. Weier (✉) · G. Gerbeth
Forschungszentrum Rossendorf,
P.O. Box 51 01 19,
01314 Dresden, Germany
e-mail: T.Weier@fz-rossendorf.de

M. Uhlemann
Leibniz Institute for Solid State and Materials Research Dresden,
P.O. Box 27 01 16,
01171 Dresden, Germany

K. Eckert
Institute of Aerospace Engineering,
Dresden University of Technology,
01062 Dresden, Germany

Keywords Magnetoelectrochemistry · Convection · Magnetohydrodynamics · Lorentz force

Introduction

The influence of magnetic fields on electrochemical reactions is already well accepted and has been reviewed several times [1–3]. However, assessments of the velocities induced by forces of magnetic origin in electrochemical cells are still scarce and, to the knowledge of the authors, limited to either flow visualizations (e.g., [4, 5]) or point velocity values inferred from the observation of tracer particles (e.g., [6–10]). The evolution of velocity measurement techniques in the last decades and especially the advent of particle image velocimetry (PIV) [11] allow for much more detailed and complete information about the flow field [12].

For a binary system with excess of supporting electrolyte, mass transport is described by the convection–diffusion equation [13]:

$$\frac{\partial c_i}{\partial t} + (\mathbf{u}\cdot\nabla)c_i = D_i\nabla^2 c_i \tag{1}$$

That is, the distribution of the concentration c_i of the electroactive component i depends on its diffusion coefficient D_i and on the velocity field $\mathbf{u}$. The momentum balance given by the Navier–Stokes equation for incompressible flow

$$\frac{\partial \mathbf{u}}{\partial t} + (\mathbf{u}\cdot\nabla)\mathbf{u} = -\frac{1}{\rho}\nabla p + \nu\nabla^2\mathbf{u} + \frac{\Delta\rho}{\rho}\mathbf{g} + \frac{1}{\rho}\mathbf{F} \tag{2}$$

contains body force terms for buoyancy $\Delta\rho\mathbf{g}$ and other force densities $\mathbf{F}$. Mass conservation is expressed by the continuity equation

$$\nabla \cdot \mathbf{u} = 0. \tag{3}$$

In the above equations, p stands for pressure, t for time, and ρ and ν for the density and kinematic viscosity of the fluid, respectively. Concentration variations cause density differences $\Delta\rho$, which in turn give rise to free convection due to the presence of gravity $\mathbf{g}$.

Depending on the material properties, different body forces of magnetic origin may exist in the solution [14]. At present, the relative importance of the Lorentz force, the paramagnetic force due to concentration gradients, and the field gradient force imposed by gradients of the magnetic field is actively discussed in the literature (e.g., [10, 15–22]). The paper at hand concentrates exclusively on the action of the Lorentz force

$$\mathbf{F}_L = \mathbf{j} \times \mathbf{B} \tag{4}$$

which is widely accepted to have a significant effect on momentum and therefore mass transfer. Owing to the experimental conditions considered in the present paper, both paramagnetic and field gradient forces can be estimated to be week in comparison to the computed Lorentz forces. The dominance of the Lorentz force is shown a posteriori based on a comparison of the experimental and numerical results.

Under conditions of common electrochemical processes, the current density is determined solely by the faradaic current to a very good approximation. In our case, the current density,

$$\mathbf{j} = \sigma(\mathbf{E} + \mathbf{u} \times \mathbf{B}) - n_i F D_i \nabla c_i \tag{5}$$

with $\mathbf{E}$ denoting the electric field strength and σ the electric conductivity, contains a term $\sigma(\mathbf{u}\times\mathbf{B})$ accounting for currents induced by the flow. For magnetic fields of moderate strength (~1 T), induced currents can usually be neglected compared to the faradaic ones (see, e.g., [27]). The rightmost term in Eq. 5 (details of the derivation can be found in [13]) accounts for the charge transport by diffusion of the electroactive species. n_i denotes the charge number of the electroactive species and F the Faraday constant. Charge transport by diffusion becomes important in case of concentration gradients, which typically evolve at electrodes and may lead to a limitation of the current by mass transfer.

The influence of Lorentz force induced convection on mass transfer described by Eqs. 1–5 has been recognized for a long time. Several equations relating the limiting current density j_l to the applied magnetic induction B_0 were proposed based on modeling and experimental data (see, e.g., [23, 24]). For the well-defined case of a horizontal channel with perpendicular electric and magnetic fields, i.e., a "magnetohydrodynamic pump electrode," Aogaki et al. [25] showed analytically and by experiment that $j_l \sim B_0^{1/3}$ holds for a boundary layer flow and $j_l \sim B_0^{1/2}$ is valid in case of the developed flow in a channel [26]. These results could later be confirmed numerically by Ngo Boum and Alemany [27].

However, different field configurations and cell geometries will result in a wide range of flow regimes and corresponding mass transfer conditions. Because the particular cell design and electrode arrangement determines the primary current distribution, it contains valuable information for the computation of the Lorentz force distribution. Unfortunately, all too often such information is omitted in the literature. Assuming a power–law relation of the type $j_l \sim B_0^m$, Kim and Fahidy [28] report a considerable spread $0.25 < m < 1.64$ of the exponents measured under different experimental conditions.

Although, as mentioned above, the Lorentz force is just one of several forces of magnetic origin, it is probably the most influential one in many cases where an electric current exists [14]. However, this might not always be so obvious. Sometimes, the vector product 4 is interpreted in a very local way (e.g., in [16, 29, 30]), only considering the field distributions in the vicinity of the electrode. Yet, the Lorentz force distribution in the whole cell volume has to be taken into account to determine the flow in the cell and thereby near the electrode.

The present paper's aim is to demonstrate that the action of the Lorentz force, which is often regarded as simple and well understood, might be surprisingly varied. Because the fluid motion in the cell is already a highly nonlinear process, detailed investigations of the field and velocity distributions should be undertaken before Lorentz force effects are finally excluded.

Materials and methods

Experimental setup

Two cylindrical cells of identical diameter and height were used in the experiments. Their dimensions and layouts are given in Fig. 1. Both cells were made from polymethylmethacrylate (PMMA) to allow easy visual access and to enable PIV measurements. The cell on the right hand side of Fig. 1 is designed to mimic experiments, which were carried out in a similar cell, horizontally aligned in uniform magnetic fields [31, 32]. PIV measurements directly in the original experimental setup of [31, 32] were prevented by the lack of optical access to the cell. To remedy this problem, a cylindrical permanent magnet was chosen for magnetic field generation.

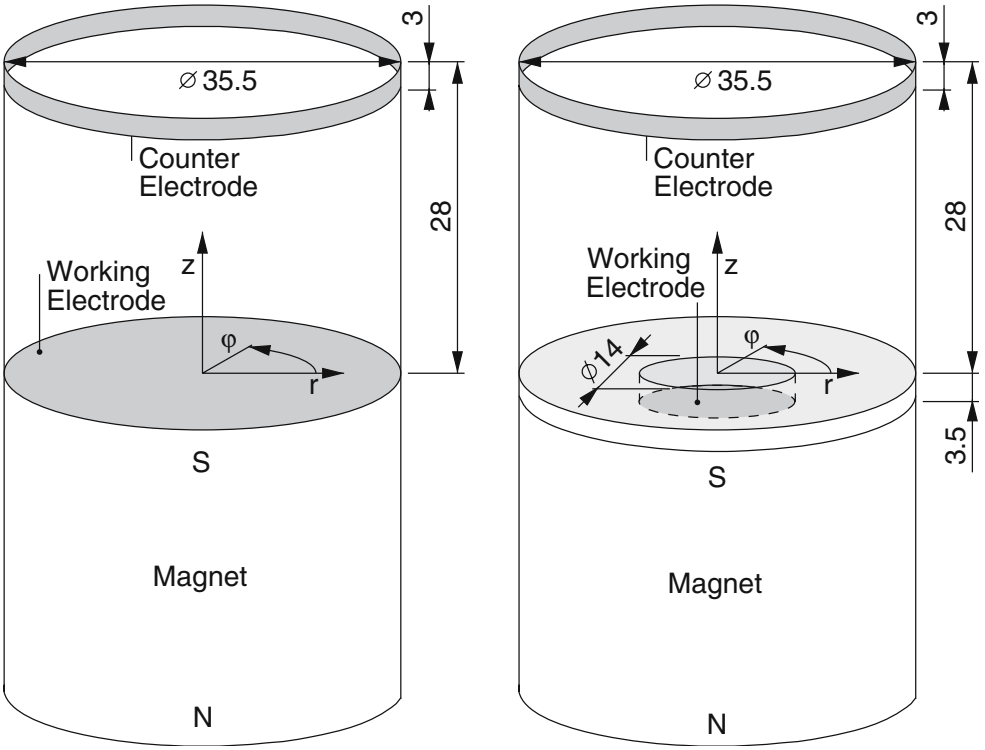

Fig. 1 Sketch of the cell with large (LWEC, *left*) and small (SWEC/, *right*) working electrode

Both cells were mounted centrically on top of this cylindrical permanent magnet consisting of a stack of six hard ferrite (SrFe) disks, each 45 mm in diameter and 9 mm in height. The bottom of the cell on the left-hand side of Fig. 1 is a copper disk, which serves at the same time as working electrode (WE). This cell will be referred to as "large working electrode cell" (LWEC) in the following.

On the right-hand side of Fig. 1, the "small working electrode cell" (SWEC) is shown. Here, the WE is placed on the bottom of a 3.5-mm-deep hole in the PMMA floor and has a diameter of 14 mm only. In both cells a copper ring, which is 3 mm in height, is mounted on top of the cells as counter electrode (CE). This arrangement had to be chosen so as not to block the optical path from the light sheet to the PIV camera (see Fig. 2).

Copper was deposited or dissoluted from aqueous solution containing 0.052 M of $CuSO_4$ and 0.073 M of Na_2SO_4 with an addition of H_2SO_4 to adjust to a pH value of 3. This leads to a conductivity of 1.8 S/m. Both the density and the kinematic viscosity of the $CuSO_4/Na_2SO_4$ solution at room temperature were experimentally determined to be ρ=1,030 kg/m^3 and $\nu=1.05\cdot10^{-6}$ m^2/s, respectively. These values were used in the numerical calculations. To facilitate the velocity measurements, a reference electrode was omitted and the experiments were run with a constant potential difference of 400 mV between WE and CE. This potential difference was chosen to avoid side reactions with gaseous products and still allow for a sufficiently high overall current density to drive a measurable flow.

Velocity fields in the r–φ plane were measured using a PCO Sensicam and a laser light sheet formed by the expanded beam of a continuous wave Ar^+-laser 2020-5 from Spectra Physics. Figure 2 shows a sketch of the setup. A density-matched fraction of polyamide powder (Vestosint 1141 from Degussa) with a mean diameter of 100 μm was used for tracer particles. Consecutive particle images taken by the camera were correlated with PIVview2C 2.3 from PIVTec to obtain the velocity vector fields. The interrogation spots were 32×32 pixels in size and had 50% overlap, resulting in a spatial resolution of 0.5 mm in axial direction. The resolution in vertical direction is determined by the 1-mm distance between consecutive measurement planes.

The magnetic field of the permanent magnet was determined by means of a three-axis probe MMZ-2512-UH and a Gaussmeter model 460 from LakeShore using an ISEL traverse for probe positioning.

Numerical approach

The distribution of the electric and the magnetic fields was calculated with the finite-element software Opera-2d from Vector Fields. For the electric field, fixed potentials corresponding to the experimentally applied potential difference at the electrodes and isolating walls were prescribed, while the magnetic field was calculated from

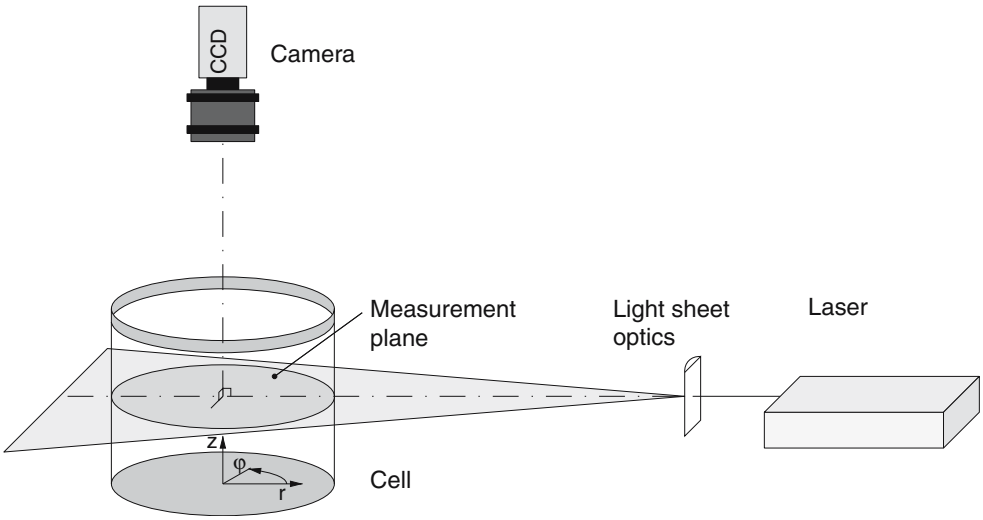

Fig. 2 Sketch of the velocity measurement setup for PIV

the total dimensions of the permanent magnet and its material properties.

Numerical simulations of the flow driven by the calculated Lorentz force were done using the Navier–Stokes equations Solver FLUENT version 6.2.16. Assuming axial symmetry and a steady flow, which is a good approximation according to the experimental results, a steady two-dimensional solution of the momentum equations in the *r*–*z* plane (cf. Fig. 1) was calculated on a structured grid of 256,000 equidistantly spaced cells. This resolution was found to be sufficient for a grid-independent solution.

In the present paper, we do not intend to provide a numerical solution to the full problem including electrochemical reactions and species transport, which is still a formidable task [33]. The numerical investigations are rather restricted to a comparison of the Lorentz force effects on the flow with the experimental findings. Therefore, a homogeneous and constant density of the electrolyte was assumed.

The no-slip wall treatment, i.e., $\mathbf{u}=0$, was applied to the bottom and the side wall, whereas the free surface was modeled by a plane of symmetry.

Because the Lorentz force acts only in azimuthal direction, it was implemented as a source term at the right-hand side of the azimuthal component of the momentum Eq. 2 using the results of the Opera-2d calculations.

Results and discussion

Field distributions

Measured and calculated values of the magnetic induction in the region inside the cell are shown in Fig. 3. As can be seen from the plot, measurement and calculation fit quite well. The field distribution (only the part from the line of symmetry (*z*-axis) to the radius of the cell is shown) is clearly an inhomogeneous one with a maximum value of 0.075 T in the center of the cell and below 0.02 T near its upper outer rim. The contours of the magnetic flux density are slightly curved as expected for the field distribution at the top of a cylindrical magnet. Magnetic field lines corresponding to these contours are given on the left-hand side of Fig. 4. Corresponding to the isocontours, they diverge toward the radius and the top of the cell.

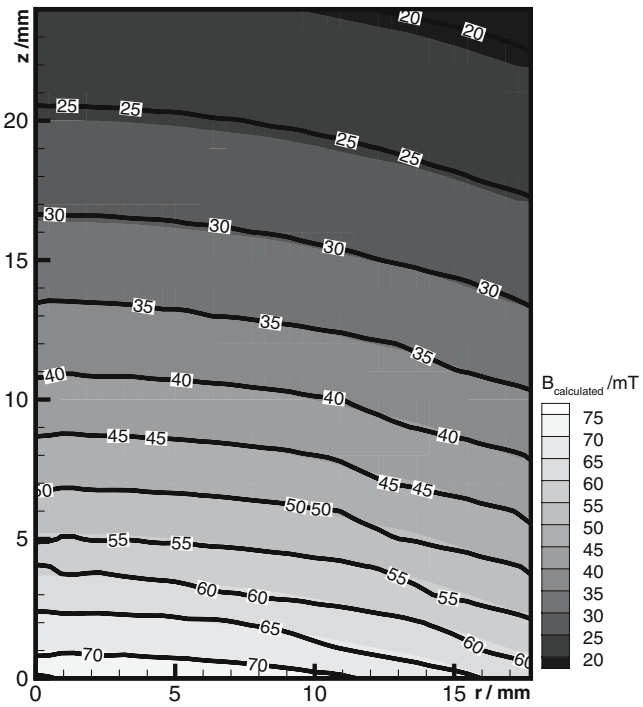

Fig. 3 Absolute value of the measured (*lines*) and computed (*filled contours*) magnetic induction

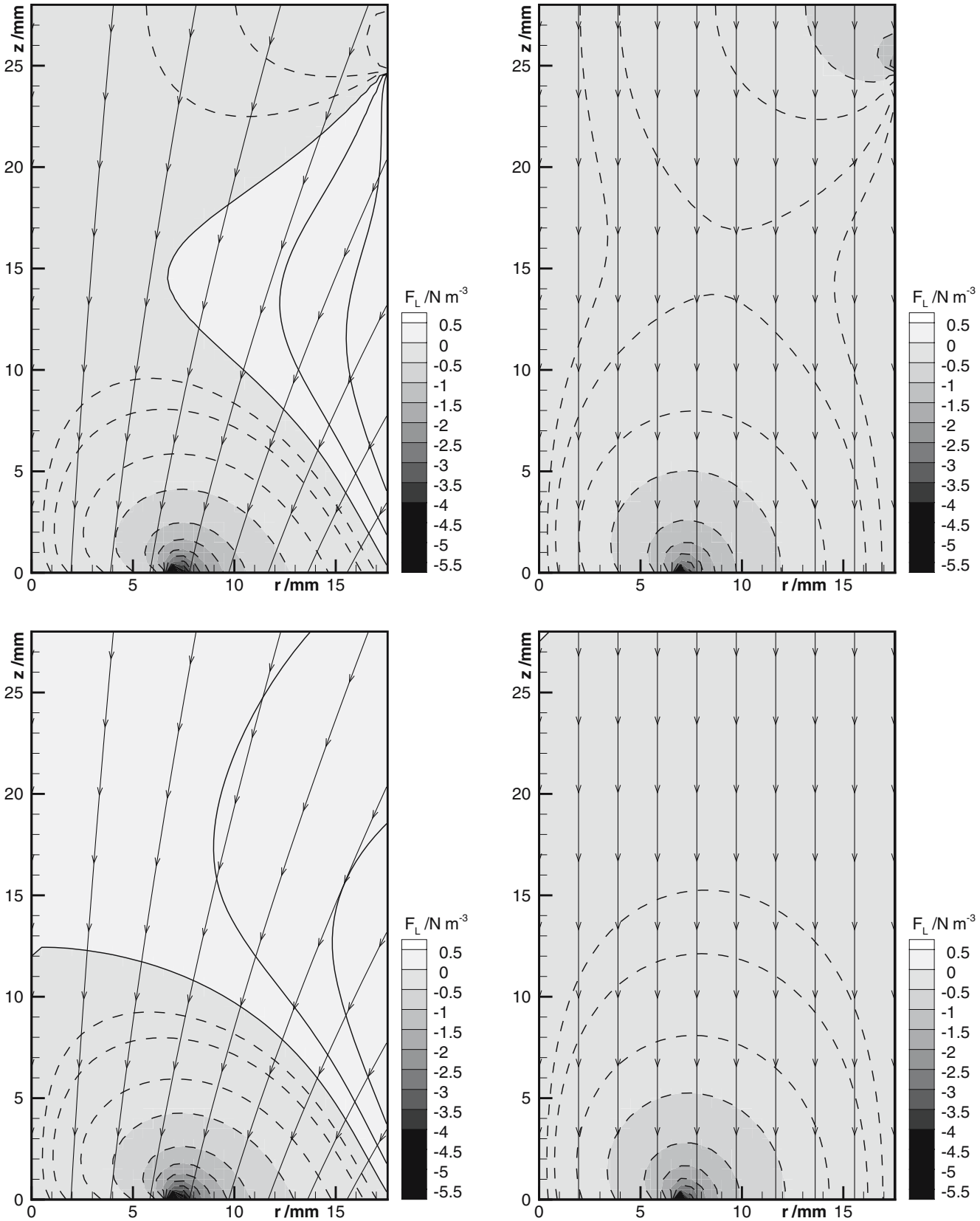

Fig. 4 Comparison of different calculated Lorentz force density distributions for the SWEC: magnetic field lines (*arrows*) and primary current density distribution corresponding to the present experimental configuration (*top left*); constant magnetic field, present primary current distribution (*top right*); present magnetic field, primary current distribution for a "lid"-electrode (*bottom left*); and constant magnetic field, primary current distribution for a "lid"-electrode (*bottom right*). *Dashed contour lines* refer to a Lorentz force in clockwise direction

The electric field lines generated by the electrode configuration in the SWEC are shown in the top-left part of Fig. 5. The ring electrode on top of the cell enforces an outward bending of the electric field lines in the uppermost part of the cell. This obviously entails crossing of electric and magnetic field lines and thereby Lorentz force generation. A second region of crossing electric and magnetic field lines is due to a strong radial component of the electric field at the bottom of the cell. At the edge of the sinking containing the small WE the electric field lines spread radially outward. The Lorentz force density in that region is stronger than in the upper part of the cell, as can be seen in the top-left diagram of Fig. 4. For a cathodically polarized WE, the Lorentz force at the force maxima points in *negative* φ direction, i.e., clockwise (marked in the figure with dashed isolines). In the right part of the cell, a region with a much weaker, but oppositely directed Lorentz force appears (marked with solid isolines). Because of the lack of optical access, PIV measurements could not have been performed inside the WE sinking. Therefore, all following discussions of the field and velocity distributions in the SWEC refer only the main part of the cell, i.e., $z>0$, and does not include the WE sinking. Note that the origin of ordinates for both cells is in the cell center and 28 mm below the upper rim of the cell, as shown in Fig. 1.

To assess the relative importance of the field deformations for the Lorentz force density distribution, it was also calculated for a homogeneous magnetic field and for a CE in the form of a lid, i.e., completely covering the top of the cell. The results are shown in the other diagrams of Fig. 4. In case of a homogeneous magnetic field and a primary current distribution imposed by the electrode configuration sketched in the right part of Fig. 2, the region of high Lorentz force density around the WE becomes more semicircular, as can be seen in the top-right diagram of Fig. 4. In addition, the area with the counterclockwise Lorentz force density disappears and the second region of higher clockwise Lorentz force density at the CE becomes more pronounced. In the bottom left diagram of Fig. 4, the magnetic field produced by the permanent magnet was combined with the primary current density distribution resulting from a CE in the form of a lid. The Lorentz force density distribution near the WE up to $z\approx10$ mm is quite similar to that in the case of the original configuration. However, the region of counterclockwise Lorentz force density is much larger now and takes up nearly all of the remaining cell volume. The field configuration belonging to the experiments by Uhlemann et al. [31, 32] results in a Lorentz force density distribution shown in the bottom-right of the diagram in Fig. 4. A homogeneous magnetic field is combined with a lid CE. Radial components of the electric field now occur only near the edge of the hole containing the WE. Due to the axial parallel magnetic field, the single remaining region exhibiting a noticeable Lorentz force density is the volume near the WE sinking. Because the electric field distribution near the cell bottom is relatively insensitive to the shape of the top electrode, the Lorentz force density distribution is quite similar to the other one with parallel magnetic field lines in the top-right of the diagram in Fig. 4.

An obvious measure to prevent the Lorentz force accumulation near the WE is to extend its radius to the total radius of the cell, i.e., to change from the SWEC to the LWEC. Therefore, electric field lines in the bottom part of the cell will become parallel to the cell axis. This can be readily seen by comparing the electric field lines in both cells shown in the two top diagrams of Fig. 5. However, the nonparallel magnetic field lines originating from the permanent magnet again give rise to Lorentz forces in the LWEC as well. Their distribution though is completely different from that in the SWEC. First, the direction of the Lorentz force in the bottom part of the cell is clockwise for the SWEC, but counterclockwise for the LWEC. Second, the Lorentz force density is concentrated in a relatively small region around the WE ($r=7$ mm) in case of the SWEC, while it monotonically increases with r and takes up considerable volume near the outer radius of the cell in the LWEC. The reason for the different circumferential direction of the Lorentz forces in both cases is the reversed role of magnetic and electric fields. In the SWEC, the radial electric field lines at the WE rim cross the magnetic field lines, which are mostly parallel to the z-axis there. With a cathodically polarized WE, the inward-pointing electric field and the downward-directed magnetic field generate a Lorentz force in clockwise direction. In contrast, the LWEC exhibits mostly axial parallel electric and magnetic fields in the cell center, while the magnetic field lines become more and more bended outward with increasing r. Thus, the downward-pointing electric field (cathodically polarized WE) is crossed by a magnetic field directed inward, resulting in an azimuthal Lorentz force in counterclockwise direction.

Velocity measurements

Small working electrode cell

Velocity measurements for the mean flow in the SWEC are shown in Fig. 6. As mentioned in the previous paragraph, only the cell volume above $z=0$ is shown because the WE sinking was not accessible by the PIV measurements. The top diagram displays contours of the azimuthal velocity component U_φ on the right and contours of the radial velocity component U_r on the left side. The distribution of U_φ follows that of the Lorentz force to a good extent: a "high-speed region" is present in the lower region of the

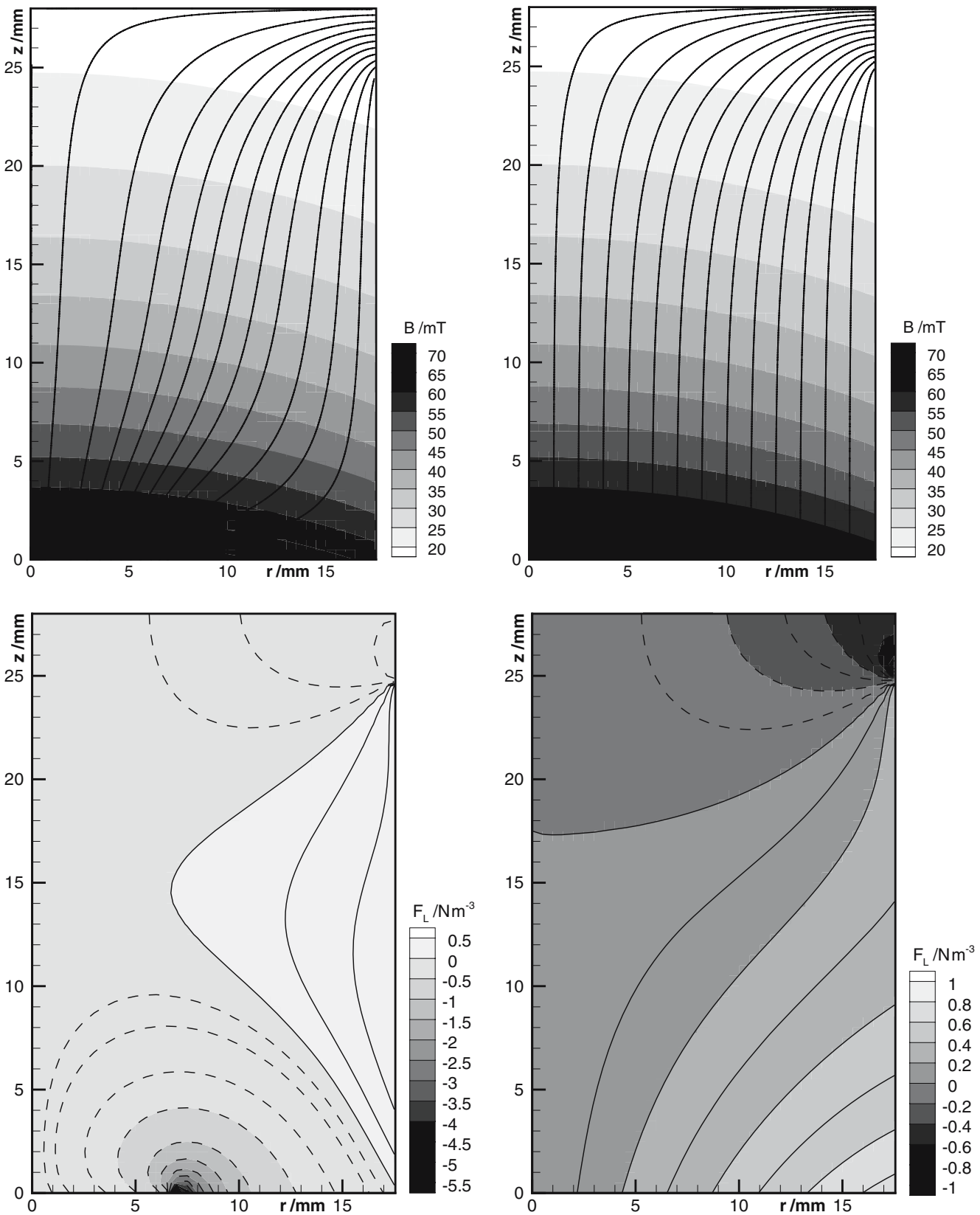

Fig. 5 Calculated magnetic induction (*isocontours*) and electric field lines (*top*) and Lorentz force density distribution (bottom) for the SWEC (*left*) and LWEC (*right*)

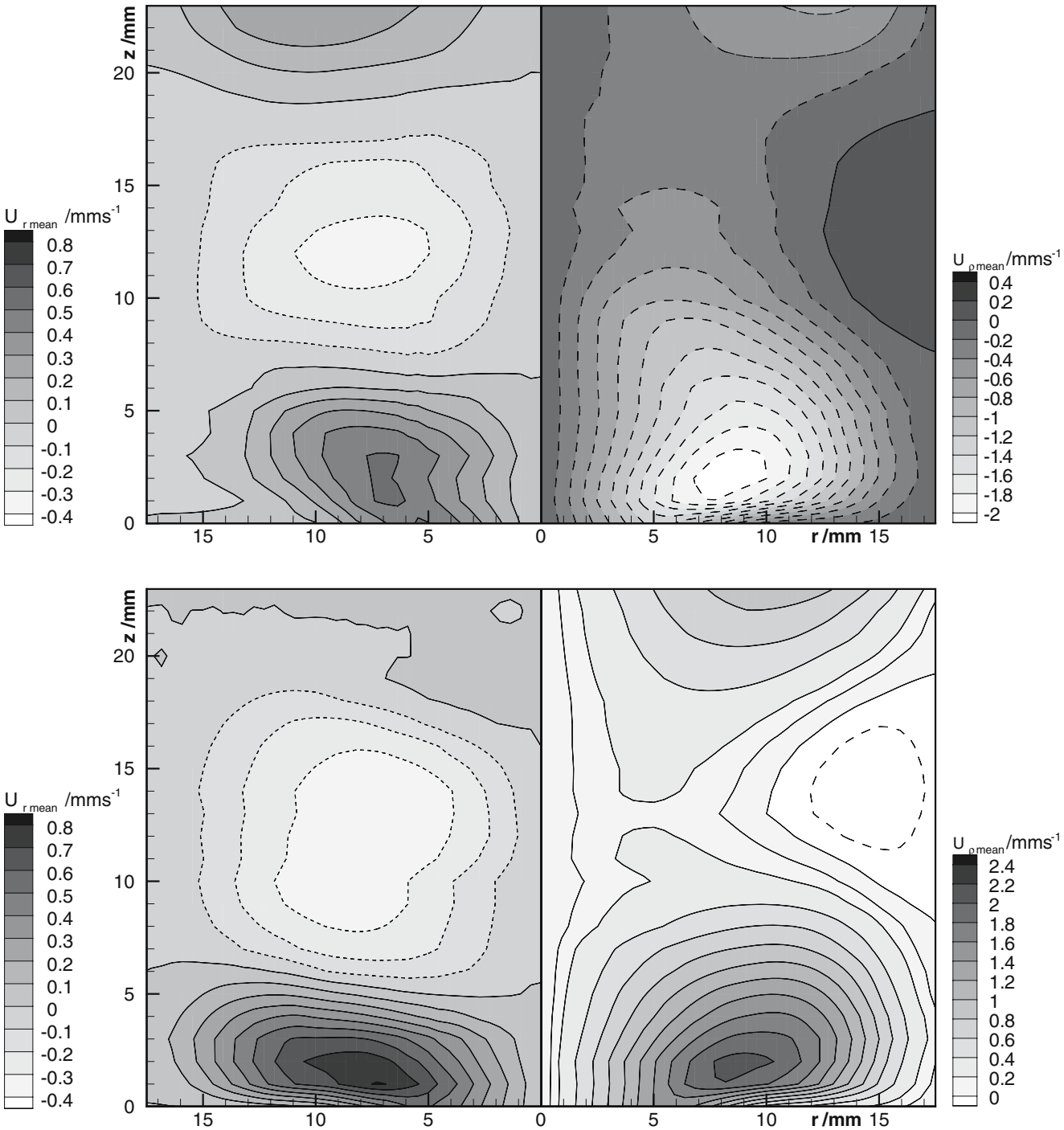

Fig. 6 Measured averaged azimuthal (*right*) and radial (*left*) velocity components in the *r–z* plane of the SWEC for an unstable density distribution (*top*) and a stable one (*bottom*)

cell where the maximum Lorentz force density is located and the azimuthal flow changes direction in the region with opposite Lorentz force. Depending on the polarity of the WE, the Lorentz force changes its circumferential direction. For a cathodically polarized WE as assumed in Figs. 4 and 5 and the top part of Fig. 6, the Lorentz force and thus the flow in the lower part of the cell is clockwise (equivalent to $U_\varphi<0$). Changing the polarity of the WE changes the direction of the electric field and thereby that of the Lorentz force. Consequently, the flow above an anodically polarized WE is counterclockwise, as can be seen in the bottom part of Fig. 6.

Besides determining the rotation direction of the azimuthal flow, the polarity of the electrodes has an influence

on the density distribution in the cell as well. If the WE is cathodically polarized, copper ions from the electrode near solution are deposited on the electrode. Therefore, the density of the electrode near electrolyte decreases and it experiences a buoyancy force, which drives it upward. At the CE, copper dissolves, leading to locally higher densities there. This heavier fluid experiences a downward force. As a consequence, an unstable density stratification, i.e., heavier fluid on top of the lighter one, is created.

The opposite is true for an anodically polarized WE. In that case, the solution near the WE is enriched by the copper dissolved from the anode. The higher density fluid is now located in the vicinity of the WE and at the bottom of the cell. At the cathodically polarized CE, copper is deposited and the lighter, depleted solution stays on top of the cell. This kind of density stratification, lighter solution on top of heavier one, is stable.

While the azimuthal flow is an immediate consequence of the azimuthal Lorentz force, as can be seen on the right-hand side of Fig. 6, a flow in radial direction is present in the cell as well. Due to the specific nature of the Lorentz force in the SWEC, showing a maximum close to the bottom wall, this secondary flow in the SWEC has a similar origin as that produced by a rotating disc. Rotating disc-driven flows, sometimes also termed "von Kármán swirling flows" [34, 35], are quite common in turbomachinery and find application at "rotating disc electrodes" [36, 37] in electrochemical investigations as well. As described, e.g., by Schlichting [38], the rotation imposed on the fluid in the vicinity of the WE exerts a centrifugal force, which throws the fluid radially outward. Due to continuity, the fluid is replaced by an axially downward motion in the center of the cell. Because the cell is not infinitely extended in radial direction but is limited by the cells' sidewalls, the outward-driven fluid has to move upward near these walls. Though the axial velocity component U_z could not have been measured directly by the present setup, it can be calculated from the experimentally determined velocity components U_φ and U_r using the continuity equation. The results of these calculations (data not shown) confirm the depicted scenario. Thus, the secondary flow in the lower half of the cylinder has the form of a toroidal vortex. Note that the secondary flow is always radially outward at the bottom of the cell, regardless of the rotational direction of the mean flow, which depends on the polarity of the electrodes.

The above discussion of density stratification in the cell allows the inferring on the direction of possible buoyancy-driven flow. In case of the cathodically polarized WE, the secondary flow on the bottom of the cell, generated by the centrifugal forces, will be opposed by the buoyancy-driven motion. The result can be seen by comparing the U_r contours on the left-hand side of Fig. 6 for the unstable (top) and stable (bottom) density stratification. In the case of the unstable density stratification, the maximum radial velocity near the PMMA cell bottom (z=0) is 0.52 mm/s. The radial location of this maximum velocity is identical to that of the maximum Lorentz force density at the rim of the WE sinking, r=7 mm. Due to the no-slip condition at the cell bottom, the axial position of the velocity maximum is shifted upward to z=2 mm. The region of outward flow does not extend to the vertical cell wall. Except in a thin layer at the PMMA cell bottom, from $r\approx$15 mm to the cell wall, a region of inward flow is detectable. This inward flow is very likely caused by the downcoming fluid. In combination with the centrifugally driven flow, it results in an additional relatively weak corner vortex, as can be inferred from the velocity distribution. Such a phenomenon is not detectable for a stable density stratification (bottom left of Fig. 6). In a region from the cell bottom up to $z\approx$5 mm, the secondary flow is solely directed outward. In addition, it is considerably stronger than in the case of the unstable density stratification. The maximum velocity amounts to 0.81 mm/s, its axial location is shifted slightly downward to z=1.5 mm, while the radial position remains at r=7 mm.

Interpreting the vortex structure in the upper part of the cell is not as straightforward as explaining the conditions near the cell bottom. If only the Lorentz force at the bottom would drive the secondary flow, the analogy with the flow in a cylindrical container with a rotating bottom should hold for all the flow features. Flows driven by a rotating end wall are usually characterized by their aspect ratio H/R and their Reynolds number $Re=\Omega R^2/\nu$ with H denoting the cylinder height, R its radius, Ω the angular velocity of the end wall, and ν the kinematic viscosity of the fluid [39]. If only a part of the bottom with the radius R_d is rotating, a third parameter R/R_d has to be taken into account [40]. For the SWEC and the flow shown in Fig. 6, a Reynolds number of approx. 14 can be calculated with the largest azimuthal velocity of 2.1 mm/s and the WE radius R_d=7 mm. Because $R/R_d\approx$2.5, the Reynolds number calculated with the cell radius would be ca. 35. For these Reynolds numbers and an aspect ratio of $H/R\approx$1.6, the secondary flow in a cylinder with a free surface driven by a rotating bottom shows only one main vortex. The first deviation from this flow topology consists in the formation of a vortex breakdown bubble on the axis of symmetry. However, at $H/R\approx$1.6, such a bubble appears first for $Re>$ 780...850 [41–43], i.e., at least an order of magnitude higher than that found in the present configuration. If the radius of the rotating disk R_d is smaller than that of the cylinder bottom, a second vortex may appear. Piva and Meiburg [40] showed this in their investigation for R/R_d=3.33, H/R=1, and a Reynolds number of 900. This Reynolds number is based on R_d as characteristic length. However, the second vortex of Piva and Meiburg [40] occurs not on top of the

first one, as observed in the SWEC, but appears between the first vortex and the cylinder sidewall. Schwiderski and Lugt [44] investigated swirling flows driven by a rotating disk and a cylinder of different rotation speed and/or direction. Although they found parameter ranges where more than one recirculation cell appears in the meridional (r–z) plane, the velocity ratios in the SWEC do not belong to these ranges.

Apparently, the Lorentz force in the direct vicinity of the PMMA cell bottom alone is not able to explain all the features of the secondary flow. Therefore, the distribution of the Lorentz forces density in the upper part of the cell, albeit much weaker than near the bottom, has to be taken into account. For the sake of easier comprehension, however, this topic will be postponed to a discussion of the flow in the LWEC.

Large working electrode cell

This flow is shown in Fig. 7. As discussed above and displayed in Fig. 5, the Lorentz force density distribution driving the flow is quite different from that in the SWEC. Consequently, the flow driven by this Lorentz force configuration differs considerable from the flow in the SWEC. The first thing to note is a considerable discrepancy in the velocities of the primary azimuthal flow found in the case of a cathodically polarized and an anodically polarized WE. At r=15 mm and z=5 mm, roughly the place of the velocity maximum in both cases, U_φ=3.3 mm/s is measured for the cathodically polarized WE and U_φ=−1.9 mm/s for the anodically polarized WE. Because changing the polarity of the WE changes the direction of the current density, the sign of the Lorentz force and thereby of the velocity is reversed, but such a notable difference of the absolute values was not observed in the SWEC. The possible reason for the finding is the occurrence of a limiting current on the CE. Due to the restrictions imposed by the requirements of the optical flow measurement, the area of the CE is only about 334 mm^2. This is still larger than the area of the WE (196 mm^2) in the case of the SWEC, but amounts to only a third of the WE area (990 mm^2) of the LWEC. Unfavorable convection conditions may therefore lead to a relatively low current at the CE and, as a consequence, also to a visibly decreased current at the WE. This smaller current generates a weaker Lorentz force density and that, in turn, results in a reduced velocity of the primary flow.

Contrary to the primary flow in the SWEC where a small portion of the electrolyte in the vicinity of the WE rotates distinctly faster than the rest of the solution, in the LWEC, a large volume of electrolyte, approx. the lower three quarter of the cell volume (Fig. 7, top right), performs nearly a solid body rotation.

Bödewadt [45] was the first who solved the Navier–Stokes equations for the fundamental case of a fluid in solid body rotation above an infinitely extended wall. Recent numerical simulation on the flow structure driven by an azimuthally directed Lorentz force in cylinders of different aspect ratio were performed in [46, 47 and references therein]. For such flows, an equilibrium between radial pressure gradient and centrifugal forces exists in the body of the rotating fluid. This equilibrium is disturbed near the wall because the flow has to slow down there to meet the no-slip condition and forms a boundary layer. Due to the slower motion, centrifugal forces are reduced, but the pressure field imposed by the core flow remains essentially the same. Thus, near the wall, a pressure-driven radial inflow is generated. Owing to continuity, this inflow results in an axially upward flow.

A radial inward flow in the vicinity of the cell bottom can be seen as well in the top diagram of Fig. 7 (left), displaying the meridional plane of the LWEC with unstable density stratification, i.e., a cathodically polarized WE. In this case, natural convection tends to support the pressure-driven secondary flow because heavier fluid from the CE moves downward near the wall and the copper-depleted fluid from the bottom experiences buoyancy. The maximum inward velocity near the cell bottom occurs at r=13 mm and z=1 mm with U_r=0.64 mm/s.

In the case of the stable density distribution due to the anodically polarized WE (Fig. 7, bottom), a region of radial inward flow still exists, but only in a very shallow layer within z<1 mm and r>12 mm and the cell walls. This inward flow is not supported by heavier fluid from the CE sinking down near the wall; therefore, it is fairly weak and will cause only a small vortex in the corner. Instead of flowing inward, the bottom near the fluid in the cell center moves radially outward. Obviously, this outward motion cannot be explained in analogy to the case of a rotating fluid above an infinitely extended disk. Again, as reasoned in the discussion of Fig. 6, the conditions in the whole cell have to be taken into account.

Looking at the azimuthal velocity distribution along a line near the wall and parallel to the cell axis, it appears that U_φ steadily declines from z=5 mm to z≈20 mm. With the same arguments used for the fluid rotating above a stationary disc, we can assume equilibrium of pressure and centrifugal forces in the bulk of the fluid and domination of the pressure gradient in the boundary layer at the sidewall. This pressure gradient will give rise to an upward flow, which in turn causes, by virtue of continuity, outward flow near the bottom and inward flow in the upper part of the cell. In the uppermost part of the cell, the primary azimuthal flow changes direction; therefore, pressure passes through a minimum. This reverse pressure gradient will drive a downward flow near the sidewall in a small region directly beneath the free surface, leading to an additional and relatively flat vortex there. This vortex

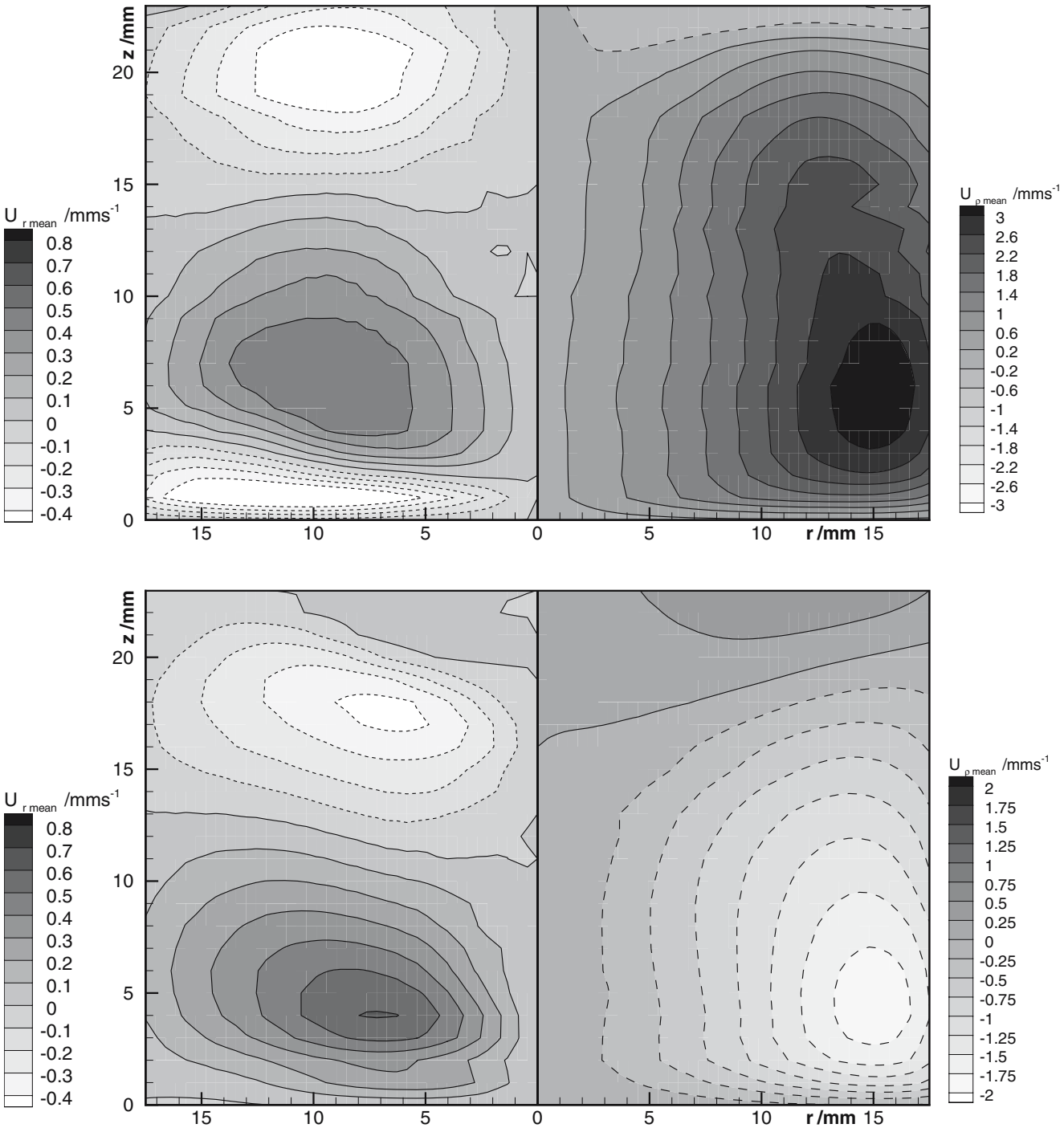

Fig. 7 Measured averaged azimuthal (*right*) and radial (left) velocity components in the *r–z* plane of the LWEC for an unstable density distribution (*top*) and a stable one (*bottom*)

features an outward flow directly at the free surface and an inward flow on its lower boundary. However, due to the axial extension of the CE and its opacity, measurements in the region $z>23$ mm were not possible. Therefore, only a very small region ($r>15.4$ mm and $z>22.5$ mm) with outward velocity is visible in the top diagram of Fig. 7 supported by the numerics later on.

Going back to the discussion of the secondary flow shown on the left-hand side of Fig. 6, its features may now be explained based on the arguments used above. Again, any axial gradient in the swirl, i.e., in U_φ, gives rise to a meridional recirculation (Davidson [48]). Thus, due to the axial variations of U_φ, two pressure maxima are generated: A first one near the corner between PMMA bottom and cell

wall and a second one near the corner formed by the cell wall and the free surface. The first maximum drives an upward flow near the wall. In contrast to the LWEC, the direction of the secondary flow near the bottom is outward in the SWEC, thus reinforcing the upward flow at the cell wall. The second maximum is responsible for a downward flow near the upper cell sidewall.

Where the downward and upward flow meet, a radially inward flow is generated, as can be seen in the left part of Fig. 6. As a consequence, the meridional flow features two recirculation regions. Their axial extension depends on the density stratification imposed by the electrochemical reaction. In case of a stable density stratification, the downward flow on top of the cell is not supported by buoyancy; therefore, the upper recirculation region is relatively small. In contrast, if natural convection intensifies the downward flow, as is the case for the unstable density stratification, the upper recirculation region increases in strength and size as can be inferred from the velocity contours on the top left part of Fig. 6.

Computation of the flow field

Results of the numerical calculation of the flow driven by the Lorentz configurations for the SWEC and LWEC are shown in Figs. 8 and 9, respectively. As remarked above, a uniform density of the solution was assumed in the numerics and electrochemical reactions are not accounted for. Thus, the flow displayed in the diagrams is the sole result of the imposed Lorentz force distribution. For the sake of easier comparability, experimental results for the azimuthal (top) and radial velocity component (bottom) were added on the left-hand side of the figures. To facilitate the understanding of the meridional flow, selected streamlines were inserted into the numerical results.

Figure 8 shows the flow in the SWEC. The double vortex system described above can be easily recognized in the numerically calculated secondary flow. Overall, experimental and numerical velocity fields of the primary flow match quite well. In detail, both azimuthal and radial velocity component are slightly overpredicted with numerically calculated velocity maxima of U_φ=2.5 mm/s at r=9 mm, z=2 mm and U_r=0.91 mm/s at r=8 mm, z=3 mm. The corresponding experimentally determined values are U_φ=2.1 mm/s at r=8 mm, z=2 mm and U_r=0.81 mm/s at r=7 mm, z=1.5 mm. Likewise, the clockwise flow around z=15 mm shows a slightly higher speed of U_φ=−0.25 mm/s at r=14.5 mm, z=15 mm for the numerics than U_φ=−0.19 mm/s at r=15 mm, z=14 mm in the experiment. Compared to the numerical results, the region of maximum radial inflow is elongated in axial direction in the experiment. Its maximum value of U_r=−0.38 mm/s at r=8 mm, z=12 mm is, however, smaller than the numerically determined U_r=−0.45 mm/s at the same position. Different from the experiment, the numerical velocity distribution was calculated for the flow above a flat bottom at z=0 without the WE sinking present in the experiment. Therefore, the velocity contours in the numerics do not intersect the r-axis. From the experimental results, however, it is obvious that azimuthal and radial flow extend into the sinking containing the WE.

Fig. 8 Comparison of experimental results (*left*) with computations (*right*) for the azimuthal velocity component (*top*) and the radial velocity component (*bottom*) of the stable flow configuration in the SWEC

The comparison of the numerical results for the LWEC with the experimental velocity distribution determined for the case of unstable density stratification is shown in Fig. 9. Again, the overall impression is a good match between experimental and numerical results for the primary flow. In this case, the velocity maximum near the wall is slightly underpredicted in the numerics with U_φ=3.0 mm/s at r=13 mm, z=6 mm compared to the experimental value of U_φ=3.3 mm/s at r=15 mm, z=6 mm. The radial inflow near the bottom is noticeably stronger in the experiment with U_r=−0.65 mm/s at r=10 mm, z=1 mm than in the numerics with U_r=−0.25 mm/s at r=12 mm z=1 mm. This is in all probability due to the natural convection-driven downflow at the cell wall, which intensifies the pressure-driven inward flow at the cell bottom. The effect does not only increase the maximum inward velocity by a factor of about 2.5, but markedly stretches the inflow region until the cell axis. Therefore, the recirculation in the lower part of the cell is enhanced at the expense of the secondary flow in the upper part of the cell. The measured maximum inflow velocity in the upper part of the cell U_r=−0.53 mm/s at r=9 mm, z=21 mm is approx. 30% smaller than the numerical determined by one of U_r=−0.79 mm/s at r=9 mm, z=21 mm. In addition, the area of higher velocity is considerably smaller in the case of the experiment. Although the experimentally determined outflow velocity in the lower part of the cell U_r=0.50 mm/s at r=10 mm, z=6.5 mm is smaller than the numerically calculated one of U_r=0.55 mm/s at r=9 mm z=6.5 mm, the volume flux in the experiment will be higher due to the larger area of high velocity.

Comparing the experimental velocity fields of Figs. 8 and 9 to the numerically treated case without density gradient, it appears that the overall effect of stable density stratification is to reduce the axial extension of the flow structures, while they are vertically elongated in the case of unstable density stratification.

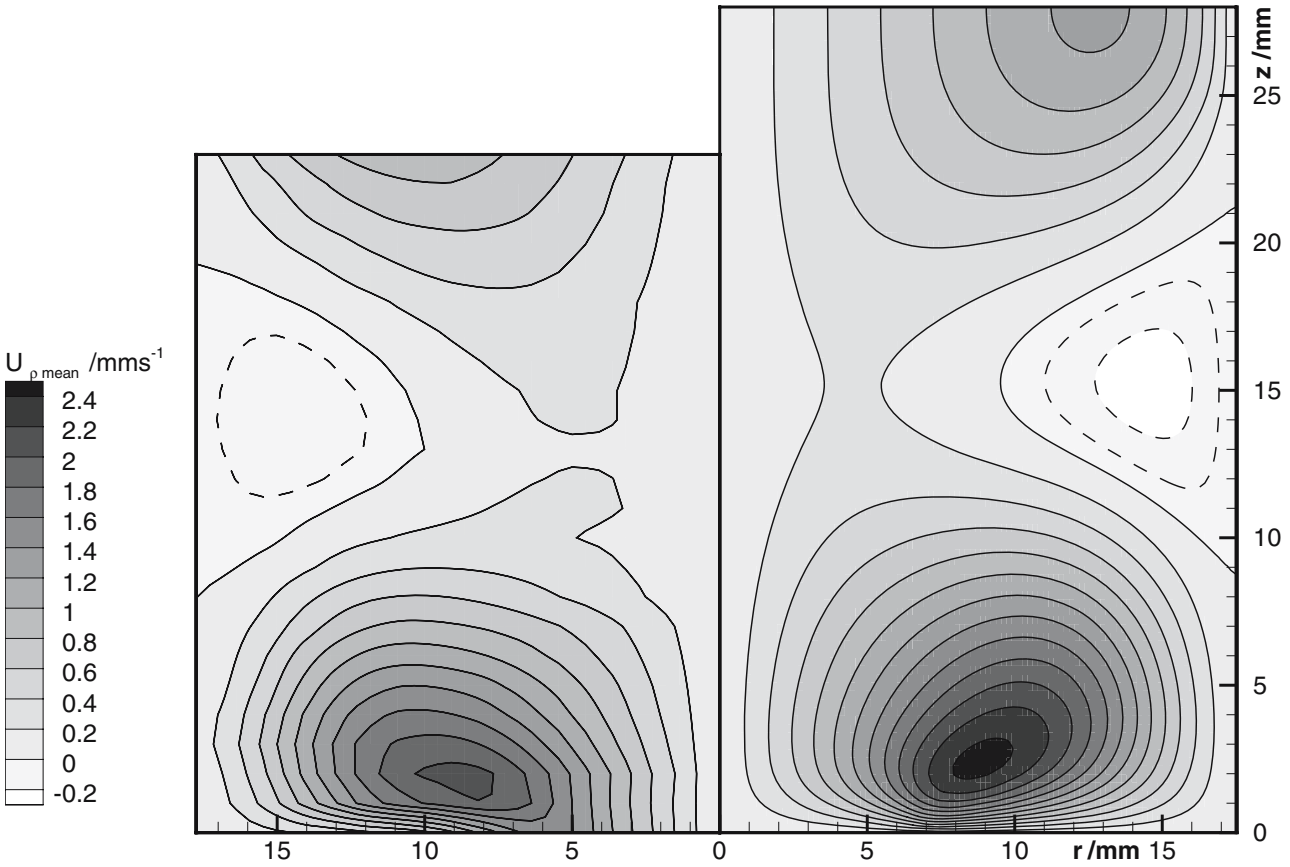
U ρ mean /mms-1
2.4
2.2
2
1.8
1.6
1.4
1.2
1
0.8
0.6
0.4
0.2
0
-0.2
z /mm
25
20
15
10
5
0
15
10
5
0
5
10
r /mm 15

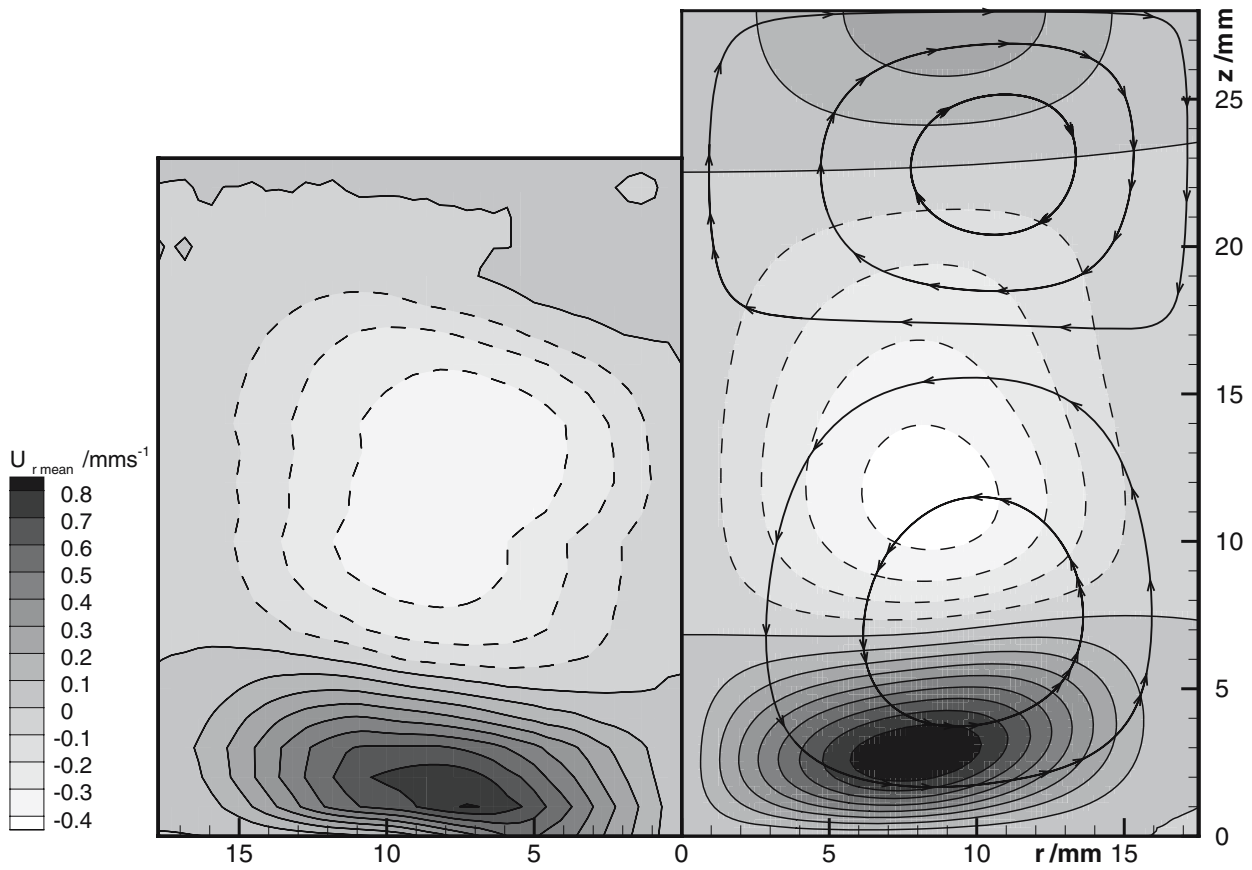
U r mean /mms-1
0.8
0.7
0.6
0.5
0.4
0.3
0.2
0.1
0
-0.1
-0.2
-0.3
-0.4
z /mm
25
20
15
10
5
0
15
10
5
0
5
10
r /mm 15

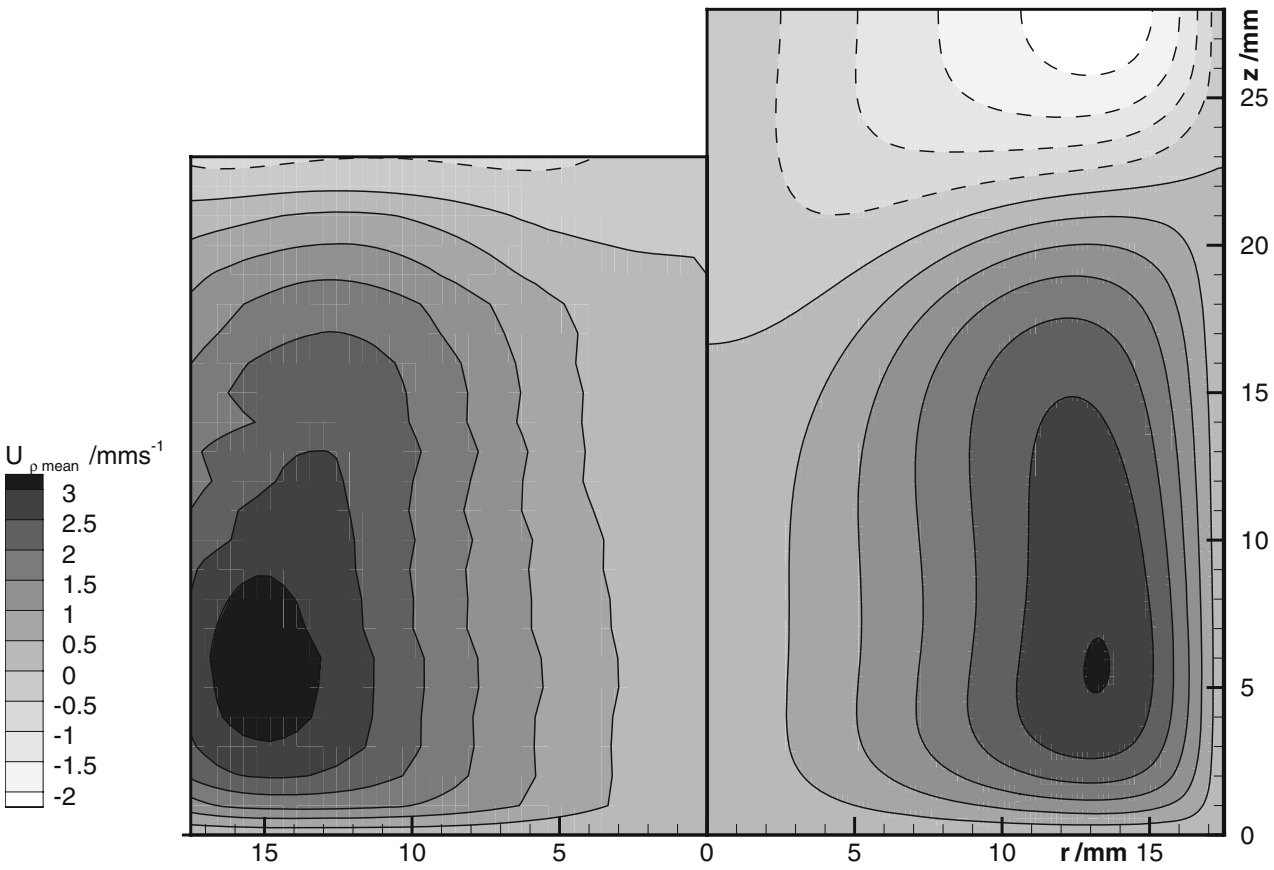
U ρ mean /mms-1
3
2.5
2
1.5
1
0.5
0
-0.5
-1
-1.5
-2
z /mm
25
20
15
10
5
0
15
10
5
0
5
10
r /mm 15

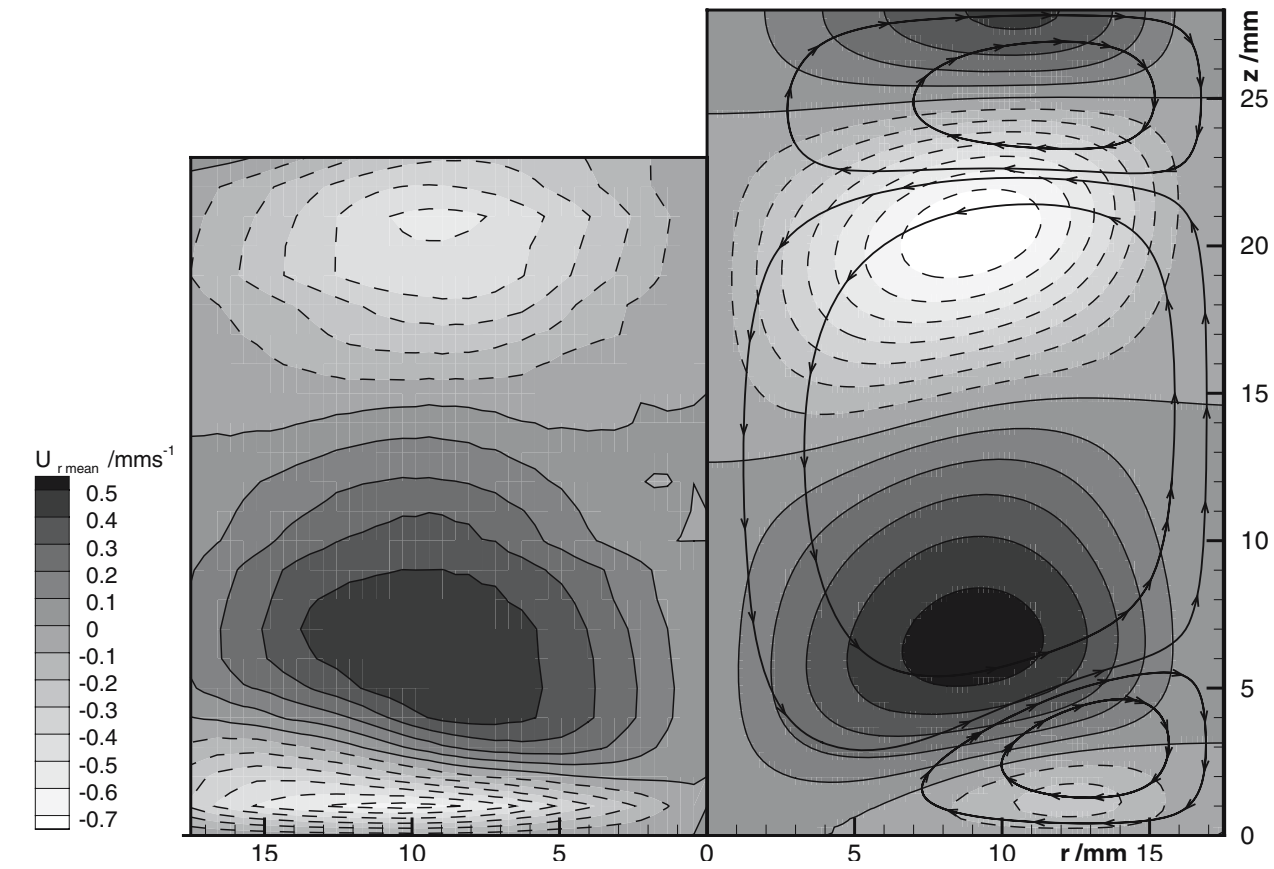
U r mean /mms-1
0.5
0.4
0.3
0.2
0.1
0
-0.1
-0.2
-0.3
-0.4
-0.5
-0.6
-0.7
z /mm
25
20
15
10
5
0
15
10
5
0
5
10
r /mm 15

◀ **Fig. 9** Comparison of experimental results (*left*) with computations (*right*) for the azimuthal velocity component (*top*) and the radial velocity component (*bottom*) of the unstable flow configuration in the LWEC

Conclusions

Complex Lorentz force density distributions may arise from seemingly simple constellations of electric and magnetic fields. These Lorentz force distributions in turn lead to complex flow structures. It is particularly emphasized that the Lorentz force-induced motion of the electrolyte dominates even in such configurations where the electric and magnetic fields are, in a first sight, seemingly parallel. Simple field inhomogeneities, such as the edges of electrodes or permanent magnets, give rise to a nonvanishing Lorentz force, which to a large extent, determine the flow field in the whole cell.

This was shown for the Lorentz force-driven flow during copper electrolysis in two cylindrical cells. Experimentally determined and numerically calculated velocity fields match reasonable well. Remaining differences between the experimental and numerical results can plausibly be explained by the action of natural convection, which was not accounted for in the numerics. Except of the Lorentz force, no other force of magnetic origin was used in the calculations, implying that the former alone is sufficient to explain the main flow features.

The secondary flow in the meridional plane depends strongly on the pressure distribution imposed by the Lorentz force-driven primary flow. Due to its relatively low velocity, this secondary flow is especially sensible to the influence of additional natural convection and density stratification. The secondary flow near the PMMA bottom of the SWEC can be understood in analogy to that driven by a rotating disk. In the LWEC, the driving mechanism for the bottom near the secondary flow is similar to that due to a fluid mass rotating above a fixed wall.

Acknowledgements Thanks are due to Jürgen Hüller for assistance with the electrochemical setup and the preparation of the solutions. We are indebted to Christophe Vallée for lending out the PCO camera. Financial support from Deutsche Forschungsgemeinschaft in frame of SFB 609 is gratefully acknowledged.

References

1. Fahidy TZ (1983) J Appl Electrochem 13:553
2. Tacken RA, Janssen LJJ (1995) J Appl Electrochem 25:1
3. Fahidy TZ (1999) The effect of magnetic fields on electrochemical processes. In: Conway BE (ed) Modern aspects of electrochemistry, no. 32, Kluwer/Plenum, New York, pp 333–354
4. Gu ZH, Fahidy TZ (1987) J Electrochem Soc 134:2241
5. Lau A, Fahidy TZ (1989) J Electrochem Soc 136:1401
6. Gak EZ (1967) Elektrokhimiya 3:89
7. Sunderman R, Fahidy TZ (1976) J Appl Electrochem 6:89
8. Mohanta S, Fahidy TZ (1978) J Appl Electrochem 8:5
9. O'Brien RN, Santhanam KSV (1987) Electrochim Acta 32:1679
10. O'Brien RN, Santhanam KSV (1990) J Appl Electrochem 20:427
11. Raffel M, Willert C, Kompenhans J (1998) Particle image velocimetry: a practical guide. Springer, Berlin Heidelberg New York
12. Weier T, Hüller J, Gerbeth G, Weiss F-P (2005) Chem Eng Sci 60:293
13. Newmann, J (1991) Electrochemical systems. Prentice-Hall, Englewood Cliffs
14. Landau L, Lifschitz E (1985) Elektrodynamik der Kontinua. Akademie Verlag, Berlin
15. Waskaas M (1993) J Phys Chem 97:6470
16. Ragsdale SR, Grant KM, White HS (1998) J Am Chem Soc 120:13461
17. Waskaas M, Kharkats YI (1999) J Phys Chem B 103:4876
18. Hinds G, Coey JMD, Lyons MEG (2001) Electrochem Commun 3:215
19. Leventis N, Gao X (2001) Anal Chem 73:3981
20. Pullins MD, Grant KM, White HS (2001) J Phys Chem B 105:8989
21. Waskaas M, Kharkats YI (2001) J Electroanal Chem 502:51
22. Leventis N, Gao X (2002) J Am Chem Soc 124:1079
23. Aaboubi O, Chopart JP, Douglade J, Olivier A, Gabrielli C, Tribollet B (1990) J Electrochem Soc 137:1796
24. Leventis N, Chen N, Gao X, Canalas M, Zhang P (1998) J Phys Chem B 102:3512
25. Aogaki R, Fueki K, Mukaibo T (1975) Denki Kagaku 43:509
26. Aogaki R, Fueki K, Mukaibo T (1976) Denki Kagaku 44:89
27. Ngo Boum GB, Alemany A (1999) Electrochim Acta 44:1749
28. Kim K, Fahidy TZ (1995) J Electrochem Soc 142:4196
29. Chen S, Yang Y (2002) J Am Chem Soc 124:5280
30. Eftekhari A (2003) Z Phys Chem 217:1369
31. Krause A, Uhlemann M, Gebert A, Schultz L (2004) Electrochim Acta 49:4127
32. Uhlemann M, Krause A, Chopart JP, Gebert A (2005) J Electrochem Soc 152:C817
33. Olivas P, Alemany A, Bark FH (2004) J Appl Electrochem 34:19
34. von Kármán T (1921) Z Angew Math Mech 1:233
35. Zandbergen PJ, Dijkstra D (1987) Annu Rev Fluid Mech 19:465
36. Levich VG (1942) Acta Physicochimica URSS 27:257
37. Riddiford AC (1966) The rotating disk system. In: Delahay P (ed) Advances in electrochemistry and electrochemical engineering, vol. 4. Interscience, New York, pp 47–116
38. Schlichting H (1954) Grenzschichttheorie. Verlag G. Braun, Karlsruhe
39. Escudier MP (1984) Exp Fluids 2:189
40. Piva M, Meiburg E (2005) Phys Fluids 17:063603
41. Brøns M, Voigt LK, Sørensen JN (2001) J Fluid Mech 428:133
42. Spohn A, Mory A, Hopfinger EJ (1998) J Fluid Mech 370:73
43. Spohn A, Mory M, Hopfinger EJ (1993) Exp Fluids 14:70
44. Schwiderski EW, Lugt HJ (1964) Ing-Arch 34:198
45. Bödewadt UT (1940) Z Angew Math Mech 20:241
46. Nikrityuk PA, Ungarish M, Eckert K, Grundmann R (2005) Phys Fluids 17:067101
47. Nikrityuk PA, Eckert K, Grundmann R (2006) Acta Mech (in press)
48. Davidson PA (1989) J Fluid Mech 209:35